PERGAMON

International Journal of Solids and Structures 38 (2001) 1415–1431

INTERNATIONAL JOURNAL OF SOLIDS and STRUCTURES

www.elsevier.com/locate/ijsolstr

Nonlinear rate-dependent stick-slip phenomena: modeling and parameter estimation

Hoon Wee [a], Yoon Young Kim [a,*], Haeil Jung [b], Gwang Nam Lee [c]

[a] *School of Mechanical and Aerospace Engineering, Institute of Advanced Machinery Design, Seoul National University, Kwanak-Gu Shinlim-Dong San 56-1, Seoul 151-742, South Korea*

[b] *Department of Mechanical Engineering for Power, Korea University of Technology and Education, Cheonan 330-860, South Korea*

[c] *LG OTIS Elevators, Nam-Gu Juan-Dong Incheon 402-200, South Korea*

Received 16 November 1999; in revised form 29 February 2000

Abstract

This study deals with a nonlinear rate-dependent stick-slip phenomenon which may occur at a rubber-to-metal interface. This type of nonlinear behavior has been observed at the interface between the guide roller and the rail of a typical elevator in motion. The main objectives of the present study are (1) to show the significant effect of the nonlinearity, (2) to propose its mathematical model with a two-stage parameter estimation method, and (3) to suggest an efficient experimental technique for the parameter estimation.

Keywords: Nonlinear stick-slip; Rate-dependent; Modeling; Parameter estimation

1. Introduction

The motivation of the present work was to predict correctly the lateral vibration of an elevator in motion. The main source of the lateral vibration is the unevenness of guide rails. To reduce the vibration transmission to the elevator, optimal design of a guide roller assembly is most important. However, this should be preceded by realistic modeling of the vibration isolation mechanism between the guide roller systems and the rails. Although a typical guide roller system is supported by springs, a simple linear spring-mass-damper model may not be appropriate. Fig. 1 shows a schematic diagram of a guide roller system in contact with the guide rail, where the z axis is the moving direction of an elevator. Typical elevators have four guide roller systems and the plane view of a guide roller system is shown in Fig. 2.

Although research reports on the elevator vibration problems are rare, Miwa (1967) and Sissala et al. (1985) have modeled the guide roller system by a simple mass-spring-damper model. As humans are most susceptible to vibrations at a low frequency range (say, frequencies below 10 Hz: see ISO 2631, 1978) and the guide roller systems are most effective in low-frequency vibration isolation, the correct prediction of the

* Corresponding author. Tel.: +82-2-880-7154; fax: +82-2-883-1513.
E-mail address: yykim@snu.ac.kr (Y.Y. Kim).

0020-7683/01/$ - see front matter
PII: S0020-7683(00)00058-5

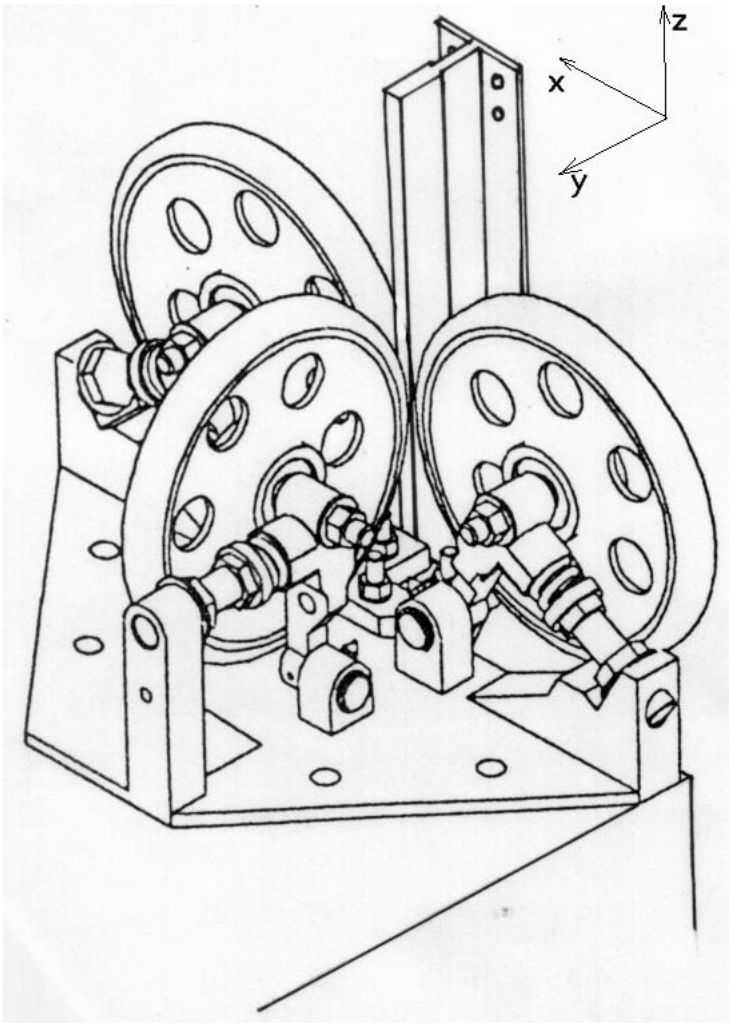

Fig. 1. A schematic diagram of a guide roller system and guide rails.

dynamic behavior of the guide rollers has been an important issue. Recent experiments (Kim and Jung, 1996) on the lateral vibrations of some elevators have exhibited some behavior that cannot be explained by the simple linear model employed by Miwa (1967) and Sissala et al. (1985). Therefore, a new nonlinear model that can predict the experimental findings needs to be developed.

The first part of this work is to report some experimental evidence for significant nonlinear behavior observed at a rubber-to-metal interface between the roller and the rail. It is shown that slipping can take place between the roller and the rail, when relative motion between them exceeds a certain limit. In addition, hysteretic damping effects of the roller tire cannot be neglected (most roller tires are made of rubber). Furthermore, rate dependence of the nonlinear behavior also needs to be considered. In order to account for this complicated behavior, an appropriate nonlinear model needs to be developed; this model should be able to describe stick-slip, and rate-dependent hysteretic phenomena.

Perhaps, the most widely used nonlinear model is the Bouc–Wen model (Bouc, 1967; Wen, 1976). The model can be used to predict various hardening or softening, and smoothly varying or nearly bilinear

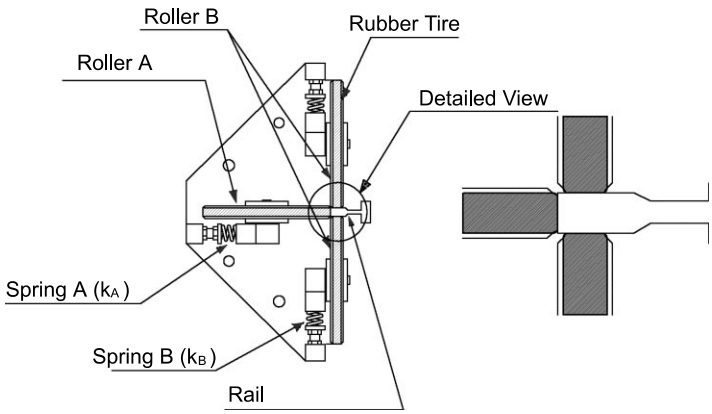

Fig. 2. A plane view of a guide roller system and guide rails.

hysteretic behavior. The performance of this model has been investigated by Baber and Wen (1981), Sues et al. (1988), and Wong et al. (1994a,b). The successful applications of this model are also reported in many situations (Michalakis and Tadibakhsh, 1985; Fertis and Lee, 1992; Ni et al., 1998). However, these investigations are restricted to rate-independent hysteretic systems in which velocity-dependent damping effects are nearly negligible. On the other hand, Tinker and Cutchins (1992, 1994) suggested a hysteretic model combined with the Coulomb friction and velocity-dependent damping in order to deal with the rate-dependent damping behavior of a wire cable isolator. However, an integer for a power of a velocity term is pre-selected in their analysis. Vinogradov and Pivovarov (1986) investigated a rate-dependent hysteretic model for vibrating cables, but no material damping was considered.

As the existing nonlinear models are not suitable to predict the complicated nonlinear phenomena occurring at the interface of the guide roller and the rail, a modified Bouc–Wen model is proposed in this work. In the present modification, a rate-dependent damping model is added to the Bouc–Wen model. However, the simple addition of two models does not give satisfactory results. Subsequently, we propose a new approach in which different force–velocity laws for each model are used and the restoring forces of each model are combined to obtain the total system restoring force. The parameters of the present modified Bouc–Wen model are estimated by employing a multi-stage estimate procedure (Yar and Hammond, 1987; Loh and Chung, 1993). Although other estimate methods (e.g., Sues et al., 1988; Chassiakos et al., 1998) may be employed, the multi-stage parameter estimation technique is more effective, when a relatively noise-free low-frequency system response is available. The present application of a two-stage parameter estimation method with the Levenberg–Marquardt method of nonlinear optimization (Fletcher, 1980) gives satisfactory results. To develop a realistic nonlinear model, we have also suggested a simple, yet very useful experimental procedure which can handle the actual excitation source such as the unevenness of a rail profile.

2. Nonlinear phenomena

Experimental results carried out for the guide roller system which is in contact with the guide roller are presented in this section. The experimental results will clearly show the nonlinear force–displacement behavior, which cannot be predicted by the simple linear model used in Miwa (1967) and Sissala et al. (1985). This section consists of static and dynamic experimental results.

2.1. Stick-slip and hysteresis

Fig. 3 shows the static experimental setup. The rail specimen is excited by a ball-screw mechanism. The reaction force by the roller system and the rail specimen displacement are measured by a load cell and a dial gage, respectively. A relation between the measured force and displacement is plotted in Fig. 4 for $k_A = k_B = 68.6$ kN/m, where k denotes the spring constant. Note that the stiffness of the guide roller system is 154.1 kN/m when the rail displacement is small, but it suddenly becomes the stiffness of spring A alone beyond a certain limit (marked by **T** in Fig. 4). When the rail displacement is small, the shearing stiffness of

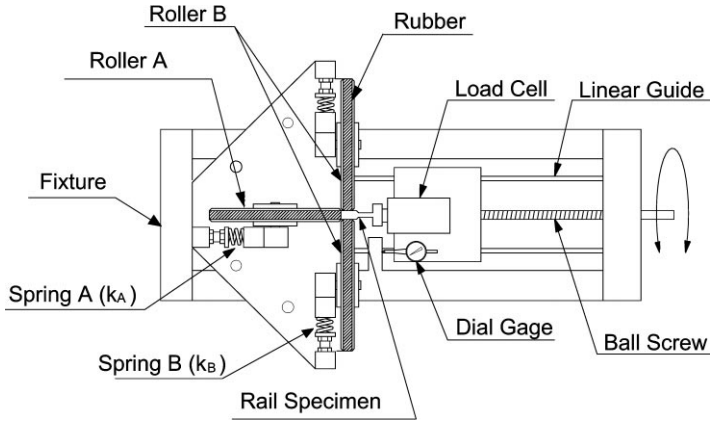

Fig. 3. An experimental setup for static analysis.

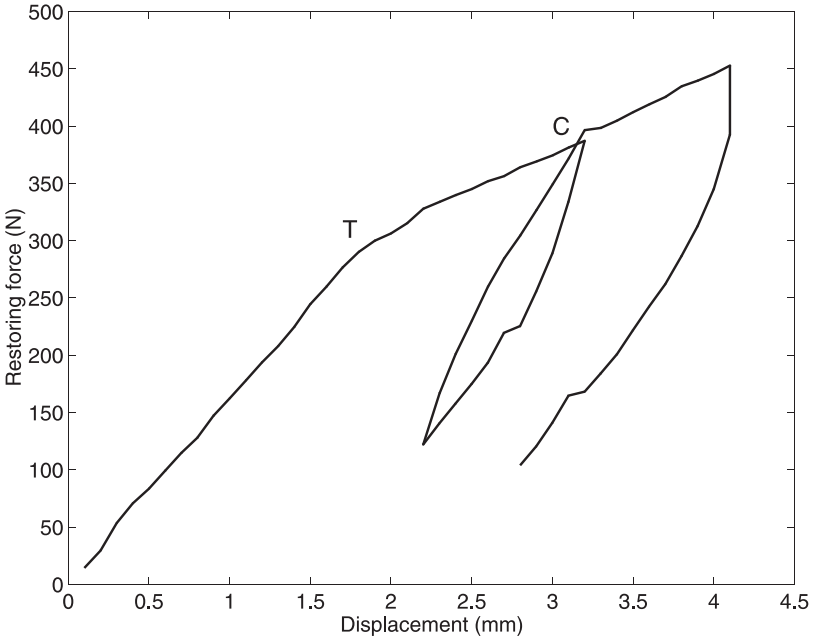

Fig. 4. Force–displacement curve from static measurement.

the tire of roller B contributes to the total stiffness of the roller system. However, slipping takes place between the tires of roller B and the rail, when the displacement increases beyond **T**.

When displacement unloading occurs, the tires of roller B stick again to the rail so that the corresponding slope in the force–displacement curve in Fig. 4 is close to the initial stiffness. If loaded again, the curve returns to **C** and then moves up with the slope of the stiffness of k_A. It is observed that the hysteresis loop during the unloading and loading is not negligible. Therefore, this material hysteresis needs to be taken into account in developing a realistic nonlinear guide roller system model. The area enclosed by the loop represents the amount of dissipated vibratory energy. To the authors' knowledge, these kinds of nonlinear stick-slip hysteresis phenomena of an elevator guide roller system are reported here first. The mathematical modeling technique of the nonlinear phenomena will be discussed later.

Before discussing the rate-dependent nature of the system response, it is also remarked that the pre-compression applied to spring B affects significantly the onset of slipping as shown in Fig. 5. The magnitude of the pre-load is equal to $k_B d$, where d is the amount of the initial deformation of spring B. For $d = 1.6$, 2.6, and 3.6 mm, the corresponding pre-loads are 117, 196, and 274 N, respectively. Fig. 5 clearly shows the delay in the onset of slipping as the magnitude of d increases. As long as the magnitude of the pre-load remains the same, the spring stiffness does not affect the onset of slipping. Fig. 6 shows the force–displacement curves for varying values of the spring stiffness ($k_A = k_B$) while the pre-load is set equal to 196 N.

Before discussing the rate-dependent phenomena that can be observed in dynamic experiments, it is now obvious that the existing linear model cannot describe the complicated nonlinear stick-slip, hysteretic phenomena.

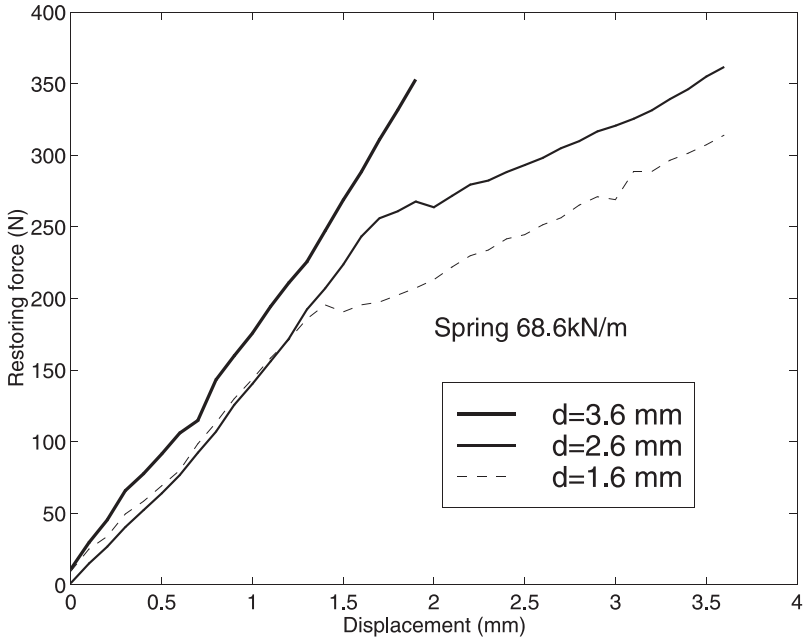

Fig. 5. The effects of the pre-load on Spring B. (The pre-load is controlled by the initial pre-deformation d of spring B.)

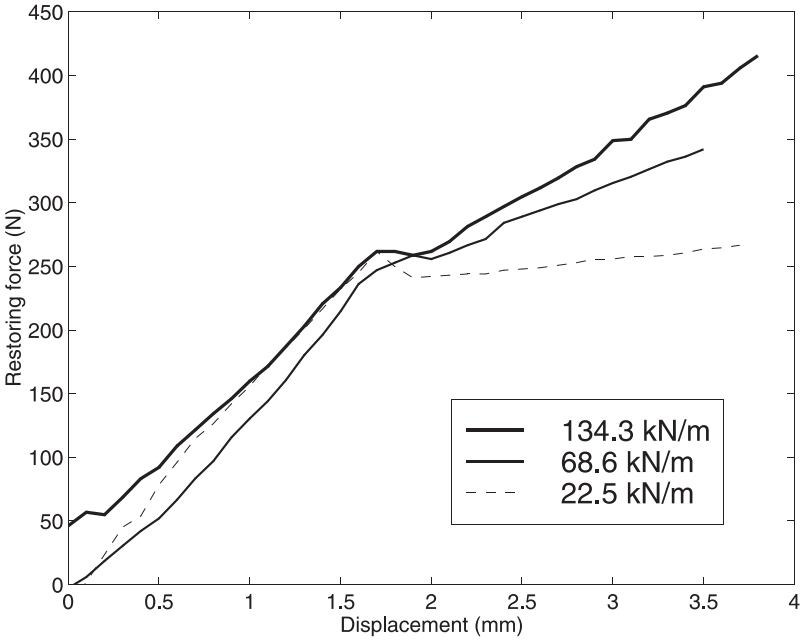

Fig. 6. The effects of the spring stiffness for the same pre-load. (The values in the figure are used for both spring A and spring B.)

2.2. Rate-dependent phenomena

The static experimental results give some insight into the nonlinear behavior of the guide roller system. However, the correct model characterizing the nonlinearity should be based on dynamic experiments, if the system response is rate-dependent. To perform dynamic experiments, the rail specimen is harmonically excited with varying frequencies. Obviously, slight modifications of the experimental setup shown in Fig. 3 are made; an AC servo motor is connected to the end of the ball screw in order to control the rail displacement precisely. An accelerometer is mounted on the rail specimen while the load cell is replaced by a force transducer. If necessary, the measured acceleration is integrated to obtain the time history of displacement.

Fig. 7 shows the force–displacement curves by harmonic displacement excitations at 3 Hz: (a) with all rollers installed and (b) with only two side rollers (roller B) installed, respectively. Not only hysteresis but also stick-slip phenomena, found in static experiments, are observed in the dynamic experiments. The area enclosed by a complete loop denotes the energy dissipated during a cycle. Comparing Fig. 7 (a) and (b), one can see that the threshold force for slipping is the same regardless of the presence of roller A. This reconfirms that slipping phenomena take place between the tire of roller B and the rail specimen and that the spring stiffness of roller A has nothing to do with the nonlinear phenomena.

Fig. 8 shows nonlinear force–displacement curves at different harmonic displacement excitations ($k_A = k_B = 68.6$ kN/m, d (pre-compression) $= 1.6$ mm). As the spring attached to roller A works only as a linear spring, only side rollers (roller B) are attached in obtaining the results shown in Fig. 8. The excitation frequencies are varied from 0.5 to 9 Hz for different displacement excitation amplitudes.

When the maximum displacements are fixed, the force level corresponding to the slip threshold increases as the excitation frequency increases. Therefore, the loop shape and the area enclosed by it change as the frequency changes; the force–displacement curve for the roller guide system is rate dependent. When the excitation frequency exceeds 5 Hz, however, the force–displacement curves tend to be insensitive to the

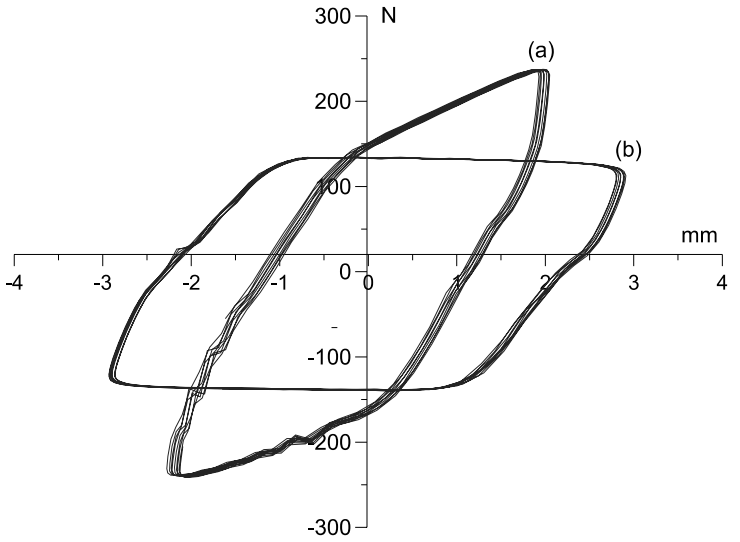

Fig. 7. Force–displacement curve: (a) with all rollers installed and (b) with only two side rollers (roller B) installed.

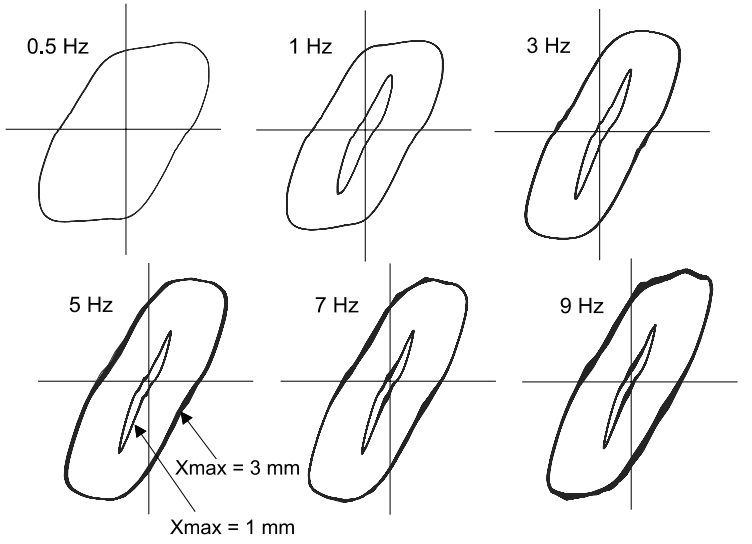

Fig. 8. Force–displacement curves at varying excitation frequencies with two different maximum displacement excitation levels (x_{max}).

excitation frequency. (Dynamic behavior below 10 Hz is of a major interest in the present investigation.) It is also observed that the shapes of the force–displacement curves are quite different depending on the maximum excitation displacement level x_{max}, which is typical of nonlinear behavior.

To summarize the findings from the dynamic experiments, we emphasize again the significant nonlinear behavior of the guide roller system; the existing linear analysis is not appropriate unless the maximum excitation displacement level is very low. We also address that the nonlinearity of the guide roller system is characterized by the coupled mechanism of stick-slip, hysteresis and rate dependence. In what follows, we propose a model that can describe the complicated nonlinearity quite satisfactorily.

3. Nonlinear model

3.1. The Bouc–Wen model

The result in Fig. 7 has confirmed that the restoring force in the system consists of the linear part by the spring of roller A and the nonlinear part from the interaction between the tires of roller B and the guide rail. Based on this observation, the following model can be used to describe the mechanics of the guide roller system:

$$f(t) = kx(t) + k_n z(t). \tag{1}$$

In Eq. (1), the total restoring force is denoted by $f(t)$ and the nonlinear restoring force is denoted by $z(t)$. The excitation displacement due to the rail unevenness is denoted by $x(t)$. No distinction between k_A and k_B is made as the same spring constant is used for both roller A and roller B, and thus, the spring constant is simply designated by k. The constant k_n is used to scale the nonlinear restoring force, so that $z(t)$ has the dimension of displacement.

As the first attempt to model the nonlinear behavior, we have employed the Bouc–Wen model without the consideration of stiffness/strength degradation as in Baber and Wen (1981). The Bouc–Wen model (Bouc, 1967; Wen, 1976) takes the following form:

$$\dot{z}(t) = \alpha\dot{x}(t) - \beta|\dot{x}(t)||z(t)|^{n-1}z(t) - \gamma\dot{x}(t)|z(t)|^n, \tag{2}$$

where $(\cdot)$ denotes the time derivative and α, β, γ and n are the model parameters to be determined. The parameter estimation scheme to determine α, β and γ including the exponent n will be given in detail in Section 3.3, but the estimated values of the parameters are given in Table 1.

Fig. 10 shows that the theoretical curves agree quite well with the experimental curves in general, but serious disagreements between the two curves near the region marked by "**C**" are observed. This discrepancy near **C** is due to the incapability of the Bouc–Wen model to describe the velocity-dependent material damping phenomenon of the tire material. However, this velocity nonlinearity cannot be ignored when system dynamic responses are of interest. Therefore, some modifications of the Bouc–Wen model are necessary, which is discussed in Section 3.2.

3.2. Generalized Bouc–Wen model

In order to consider the effects of the rate-dependent nonlinearity, we propose to incorporate the mth-power velocity damping model in the Bouc–Wen model considered in Eq. (2). The restoring force of this model is usually expressed as $c|\dot{x}(t)|^m \operatorname{sgn}(\dot{x}(t))$. Although the power m can take any positive value (Mottershead and Stanway, 1986), some previous approaches (Tinker and Cutchins, 1992, 1994) use an integer value for the exponent m and thus only the coefficient c is estimated as the model parameter to be estimated. However, both the coefficient c and the exponent m will be estimated by the two-stage parameter estimated scheme which will be described later; as will be seen, this will improve the results considerably.

Table 1
Estimated parameters

	Excitation frequency (Hz)	α	β	γ	n
Bouch–Wen model	3	0.9933	0.4123	−0.3634	4.3485
	5	1.0039	0.3872	−0.3353	3.8120
	7	1.0049	0.4829	−0.3982	3.1072
	9	1.0202	0.4829	−0.3982	3.1072

In incorporating the mth-power velocity damping model into the Bouc-Wen model, the nonlinear restoring force may be written as

$$z(t) = c|\dot{x}(t)|^m \operatorname{sgn}(\dot{x}(t)) + z_{\mathrm{BW}}(t), \tag{3}$$

where $z_{\mathrm{BW}}(t)$ designates the Bouc–Wen hysteresis model stated previously in Eq. (2). It is easier to express the model stated by Eq. (3) taking its time derivative. The advantage is that all the model parameters can appear explicitly as

$$\dot{z}(t) = c\ddot{x}(t)\left[m|\dot{x}(t)|^{m-1}\frac{\partial|\dot{x}(t)|}{\partial\dot{x}(t)}\ \operatorname{sgn}(\dot{x}(t)) + |\dot{x}(t)|^m\frac{\partial\operatorname{sgn}(\dot{x}(t))}{\partial\dot{x}(t)}\right] + \alpha\dot{x}(t) - \beta|\dot{x}(t)||z(t)|^{n-1}z(t) - \gamma\dot{x}(t)|z(t)|^n, \tag{4}$$

where $\partial|\dot{x}(t)|/\partial\dot{x}(t) = \operatorname{sgn}(\dot{x}(t))$, $\partial\operatorname{sgn}(\dot{x}(t))/\partial\dot{x}(t) = \delta(\dot{x}(t))$. The functions sgn and δ represent the signum and the impulse functions, respectively. On rewriting Eq. (5) becomes

$$\dot{z}(t) = c\ddot{x}(t)\left[m|\dot{x}(t)|^{m-1}\operatorname{sgn}^2(\dot{x}(t)) + |\dot{x}(t)|^m\delta(\dot{x}(t))\right] + \alpha\dot{x}(t) - \beta|\dot{x}(t)||z(t)|^{n-1}z(t) - \gamma\dot{x}(t)|z(t)|^n. \tag{5}$$

Eq. (5) is the coupled representation of the Bouc–Wen model and the velocity damping model. Instead of using Eq. (5), we also propose to use an alternative model. In this model, the role of velocity damping term is regarded as minor modifications of the Bouc–Wen hysteretic model:

$$z(t) = z_{\mathrm{BW}}(t) + z_{\mathrm{MD}}(t), \tag{6a}$$

where

$$\dot{z}_{\mathrm{BW}}(t) = \alpha\dot{x}(t) - \beta|\dot{x}(t)||z_{\mathrm{BW}}(t)|^{n-1}z(t) - \gamma\dot{x}(t)|z_{\mathrm{BW}}(t)|^n, \tag{6b}$$

$$\dot{z}_{\mathrm{MD}}(t) = c\ddot{x}(t)[m|\dot{x}(t)|^{m-1}\operatorname{sgn}^2(\dot{x}(t)) + |\dot{x}(t)|^m\delta(\dot{x}(t)]. \tag{6c}$$

Note that the time derivatives of $z_{\mathrm{BW}}(t)$ and $z_{\mathrm{MD}}(t)$ are not directly coupled. They are updated independently at a given time step: The performances and results from Eqs. (5) and (6a)–(6c) will be discussed in Section 4.

3.3. Parameter estimation

The system identification procedure can be defined as the estimation of the parameter vector $\{\theta\} = \{c, m, \alpha, \beta, \gamma, n\}^{\mathrm{T}}$ of the proposed model using the experimentally measured acceleration $(\ddot{x}(t))$, velocity $(\dot{x}(t))$, displacement $(x(t))$ of the rail specimen and the restoring force $(z(t))$. Considering Eq. (5), the residual function can be defined as

$$R(t) = c\ddot{x}(t)[m|\dot{x}(t)|^{m-1}\operatorname{sgn}^2(\dot{x}(t)) + |\dot{x}(t)|^m\delta(\dot{x}(t))] + \alpha\dot{x}(t) - \beta|\dot{x}(t)||z(t)|^{n-1}z(t) - \gamma\dot{x}(t)|z(t)|^n - \dot{z}(t). \tag{7}$$

The parameter estimation scheme can be divided into two stages:

(*1*) *First stage:* At this stage, the exponential powers m, n are fixed to some proper values and the other parameters are estimated through a least square scheme. Then, the residual function (7) becomes linear with respect to the remaining parameters:

$$\tilde{R}(t) = cI_1(t) + \alpha I_2(t) + \beta I_3(t) + \gamma I_4(t) - \dot{z}(t), \tag{8}$$

where

$$I_1(t) = \ddot{x}(t)[m|\dot{x}(t)|^{m-1}\,\mathrm{sgn}^2(\dot{x}(t)) + |\dot{x}(t)|^m \delta(\dot{x}(t))],$$
$$I_2(t) = \dot{x}(t),$$
$$I_3(t) = -|\dot{x}(t)||z(t)|^{n-1} z(t),$$
$$I_4(t) = -\dot{x}(t)|z(t)|^n.$$

In the case of applying Eq. (6a)–(6c), $z(t)$ must be replaced by $z_{\mathrm{BW}}(t)$, but $z_{\mathrm{BW}}(t)$ is assumed to be equal to $z(t)$ initially, as the velocity damping term is not known as yet at this stage.

The error function in the least square is simply written as

$$\tilde{E}(t) = \sum_{i=1}^{N} [cI_1(t) + \alpha I_2(t) + \beta I_3(t) + \gamma I_4(t) - \dot{z}(t)]^2. \tag{9}$$

From this stage, one set of parameters $\{c, m, \alpha, \beta, \gamma, n\}^{\mathrm{T}}$ is obtained although these parameters may not match the measured data satisfactorily. As the convergence speed of the nonlinear optimization method depends heavily on the initial guess of the parameters, the estimated parameter in this step is important for the next step.

(*2*) *Second stage:* At this second stage, the Levenberg–Marquardt method is adopted for the estimation of nonlinear system, which has proved to be more robust and efficient than the widely used Gauss–Newton method (Fletcher, 1980; Draper and Smith, 1981). The error function at the second stage can be expressed as

$$E = \sum_{k=1}^{N} R_k^2, \tag{10}$$

where N is the number of time samples and R_k is defined as

$$R_k = R(t_k) \quad (k = 1, \ldots, N). \tag{11}$$

Note that the partial derivative of E with respect to the parameter θ_i can be expressed as

$$q_i = \frac{\partial E}{\partial \theta_i} = 2\sum_{k=1}^{N} R_k \frac{\partial R_k}{\partial \theta_i} \quad (i = 1, \ldots, 6), \tag{12}$$

where $\{\theta_1, \theta_2, \theta_3, \theta_4, \theta_5, \theta_6\}^{\mathrm{T}} = \{c, m, \alpha, \beta, \gamma, n\}^{\mathrm{T}}$. The elements of the Jacobian matrix $\partial R_k/\partial \theta_i$ are given in Appendix A. The Hessian matrix is found as

$$H_{ij} = \frac{\partial^2 E}{\partial \theta_i \partial \theta_j} = 2\sum_{k=1}^{N} \frac{\partial R_k}{\partial \theta_i}\frac{\partial R_k}{\partial \theta_j} + 2\sum_{k=1}^{N} R_k \frac{\partial^2 R_k}{\partial \theta_i \partial \theta_j}. \tag{13}$$

Note that the second term contains R_k which approaches to zero as the parameters are close to the true solutions. Therefore, one may neglect this term when the residual is quite small (Fletcher, 1980). For a given set of parameters $\{\theta\}_i$, the Levenberg–Marquardt scheme searches a new set $\{\theta\}_{i+1}$ systematically from

$$\theta_{i+1} = \theta_i - [H(\theta_i) + \lambda_i I]^{-1} q(\theta_i), \tag{14}$$

where λ_i is the Levenberg–Marquardt parameter which controls both the magnitude and direction of the next iterative step.

3.4. Numerical simulation

In order to verify the validity of the proposed parameter estimation scheme stated in Section 3.3, numerical simulations are performed. To this end, numerical data for $c = 0.05$, $m = 0.6$, $\alpha = 1.0$, $\beta = 0.8$,

$\gamma = 0.2$, $n = 3$ are generated. The corresponding curve is similar to those shown in Fig. 8, but is not plotted explicitly. In generating the numerical data, a periodic displacement excitation $x(t) = x_0 \sin(\omega_0 t)$ is considered and the corresponding nonlinear restoring force by Eq. (3) is simulated. The excitation amplitude and the frequency are denoted by x_0 and ω_0, respectively. The generated discrete signals are sampled at a sufficiently large sampling rate of 200 Hz in order to avoid typical problems in discrete sampling.

To check the robustness of the estimation technique with respect to the noises, the Gaussian noises n_1 and n_2 are added to the original numerical data $x(t_k)$ and $z(t_k)$:

$$\tilde{x}(t_k) = x(t_k) + \epsilon|x(t_k)|n_1(t_k), \quad \tilde{z}(t_k) = z(t_k) + \epsilon|z(t_k)|n_2(t_k). \tag{15}$$

In Eq. (15), $\tilde{x}(t_k)$ and $\tilde{z}(t_k)$ are considered as the observed data with noise. The Gaussian noises $n_1(t_k)$ and $n_2(t_k)$ are assumed to have zero mean and variance of unity. Several values of the noise level ϵ are considered.

Using the initial guess, $m = 0.4$ and $n = 1$, the estimated results by the present approach are given in Table 2 for various noise levels. The numerical data are taken during 10 cycles of displacement excitation at 3 Hz. (Unless specified otherwise, all the numerical data are taken during 10 cycles.) Table 2 indicates that the present technique works well even for relatively large noise levels. To evaluate the performance of the present two-stage estimation technique, several excitation frequencies are considered. The estimated results given in Table 3 shows that the approach is insensitive to the excitation frequencies.

It is worth examining the effect of initial guesses of m and n on the estimated results. We consider two sets of initial guesses. In each set, either m or n is fixed while the other varies. The numerical results are summarized in Table 4 in which the noise level ϵ is taken as 1%. Table 4 shows that the results are not sensitive to the initial guesses of n, but quite sensitive to the initial guess of m. If m becomes quite larger than the true value (say, $m = 0.8$, $n = 3$), in particular, the estimated result is obsolete. This is because excessive material damping cannot be compensated by the Bouc–Wen nonlinear effect. Therefore, the use of a good initial guess of m is important. In practice, several different initial values of m need to be used for satisfactory results.

Table 2
Estimated parameters with the first-stage initial guess of $m = 0.4$ and $n = 1$

Noise level (ϵ)	c	m	α	β	γ	n
1.0%	0.0500	0.6001	0.9997	0.7914	0.2081	2.9811
2.0%	0.0502	0.5993	1.0004	0.7939	0.2067	2.9837
5.0%	0.0498	0.6104	1.0014	0.7458	0.2680	2.7803
10.0%	0.0481	0.6198	1.0025	0.6988	0.3002	2.6160
True value	0.0500	0.6000	1.0000	0.8000	0.2000	3.0000

Table 3
The effect of the excitation frequencies on the estimated results [a]

Excitation frequency (Hz)	c	m	α	β	γ	n
1	0.0500	0.6024	0.9977	0.7948	0.2029	2.9578
3	0.0484	0.6115	1.0006	0.7982	0.2028	3.0109
5	0.0492	0.6042	1.0085	0.7867	0.2171	2.9417
7	0.0491	0.6077	0.9913	0.7940	0.2070	2.9996
True Value	0.0500	0.6000	1.0000	0.8000	0.2000	3.0000

[a] The initial guess: $m = 0.4$, $n = 1$, noise level $\epsilon = 5\%$.

Table 4
The effect of initial values of m and n on the estimated results ($\epsilon = 1\%$)

Initial value		c	m	α	β	γ	n
m	n						
0.6	1	0.0500	0.6005	0.9996	0.7958	0.2049	2.9820
0.6	2	0.0500	0.6008	0.9992	0.7914	0.2096	2.9799
0.6	5	0.0502	0.5993	1.0008	0.7926	0.2101	2.9872
0.6	8	0.0499	0.6013	0.9986	0.8026	0.1973	2.9903
0.3	3	0.0502	0.5984	0.9981	0.8046	0.1925	3.0208
0.5	3	0.0501	0.5985	1.0027	0.7979	0.2017	3.0021
0.7	3	0.0501	0.6002	0.9994	0.7969	0.2040	2.9953
0.8	3	0.0718	0.6610	0.6803	94.192	−94.175	46.417
True value		0.0500	0.6000	1.0000	0.8000	0.2000	3.0000

4. Experiments and model verification

The dynamic experimental data plotted in Fig. 8 will be used to estimate the model parameters $(c, m, \alpha, \beta, \gamma, n)$, where the two-stage parameter estimation technique proposed in Section 3.3 will be used. First, we evaluate the performance of the two nonlinear models corresponding to Eqs. (5) and (6a)–(6c) and select the one which fits better the experimental data in Fig. 8. Once an appropriate nonlinear model is selected, an experimental data acquisition technique useful for actual multi-frequency excitations will be suggested.

Fig. 9 shows how accurately the two nonlinear models corresponding to Eqs. (5) and (6a)–(6c) trace the experimental data at various frequencies. The model parameters are estimated by the two-stage estimation technique. It is obvious that the model corresponding to Eq. (6a)–(6c) (will be simply called "the present model") outperforms the model corresponding to Eq. (5). This is because the rate-dependent and stick-slip nonlinearities are caused by different mechanics; the present model distinguishes rate-dependent nonlinearity from stick-slip nonlinearity, whereas the model by Eq. (5) does not. It is worth noting that the Bouc–Wen model traces the experimental results quite well except the corner **C** as shown in Fig. 10. Therefore, the rate-dependent velocity damping term should serve to make minor corrections near **C** when added to the Bouc–Wen model.

The estimated parameters for the present model are given in Table 5. Note that the variance of the estimated values for different excitation frequencies is relatively small. However, it is difficult to find a single set of parameters that can be used for multi-frequency (or general) excitations. However, typical displacement excitations have multi-frequency components as shown in Fig. 11. Fig. 11(a) shows the time history of a typical displacement excitation given to a 240 m/min elevator due to the rail unevenness (see Sissala et al., 1985). Its power spectrum is shown in Fig. 11(b). Fig. 11(b) shows that the power spectrum decreases monotonically at an approximate rate of −30 dB per decade. Therefore, this spectrum decay rate should be reflected in the parameter identification of the present nonlinear model.

To reflect the shape of the power spectrum shown in Fig. 11(b), we employ a swept-sinusoidal displacement excitation in which the amplitude of each frequency component varies with the decay rate of the power spectrum. Fig. 12(a) shows the swept-sinusoidal displacement used in dynamic experiments and Fig. 12(b) shows the measured restoring force $z(t)$. Based on the experimental data in Fig. 12(a) and (b), the parameters of the present model are estimated, which are given in Table 6. Although the estimated values of the parameters in Table 6 are not very close to those given in Table 5, the hysteresis loop

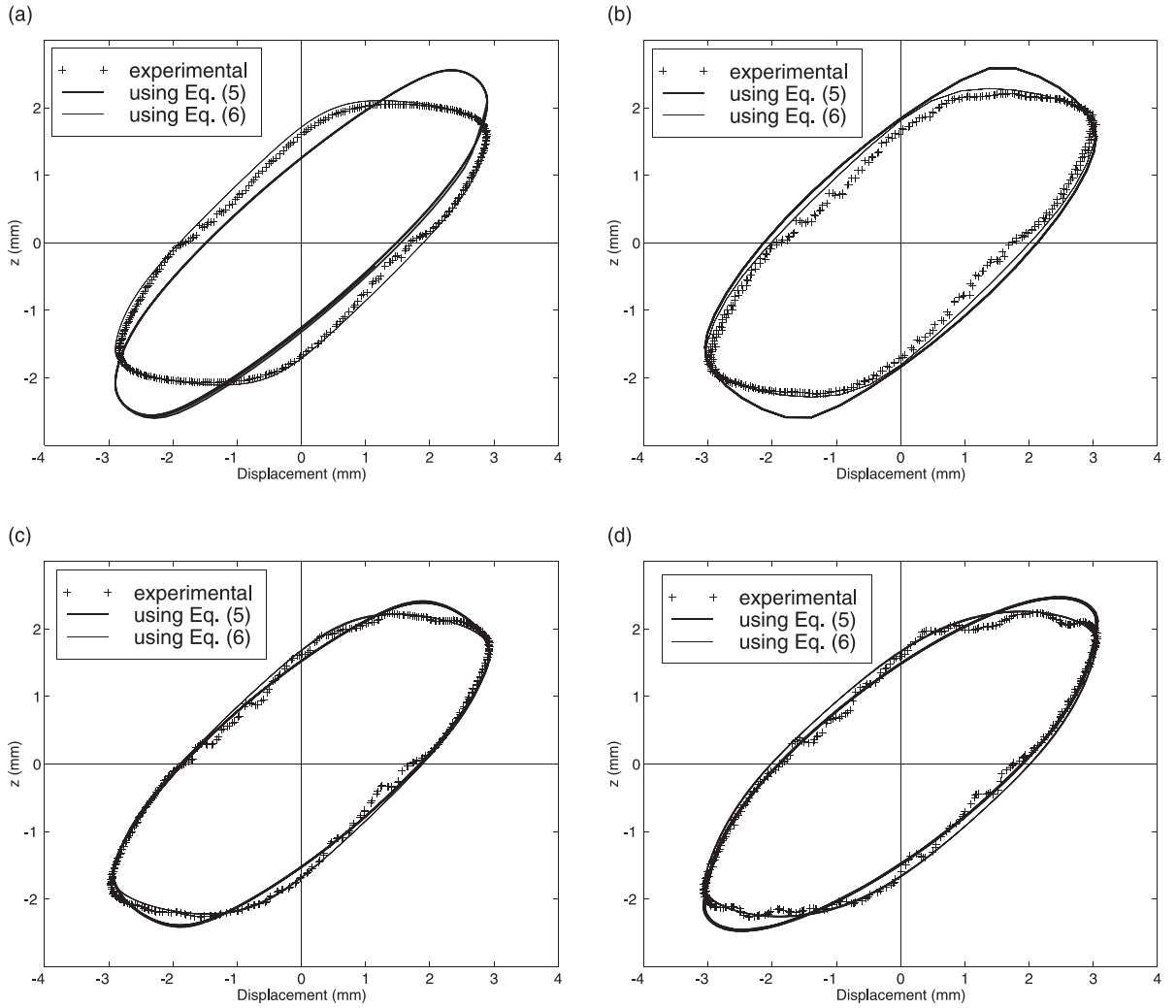

Fig. 9. The results by the two nonlinear models and experimental data: (a) for 3 Hz excitation, (b) for 5 Hz excitation, (c) for 7 Hz excitation, and (d) for 9 Hz excitation.

obtained by the present model agrees quite well with the experimentally determined hysteresis loop as shown in Fig. 12(c).

To check the accuracy of the present model, the following error measure may be used:

$$E_z = \left[\frac{\Sigma_{k=1}^{N} |z_k - \tilde{z}_k|^2}{\Sigma_{k=1}^{N} |z_k|^2} \right]^{1/2}, \tag{16}$$

where z_k and $\tilde{z}_k$ designate the measured and predicted values of the restoring force. Based on the error measure in Eq. (16), E_z is 6.41 %. If the Bouc–Wen model is used, however, E_z goes up to 12.44 %. It is clear that the present model gives quite improved results over the existing Bouc–Wen model.

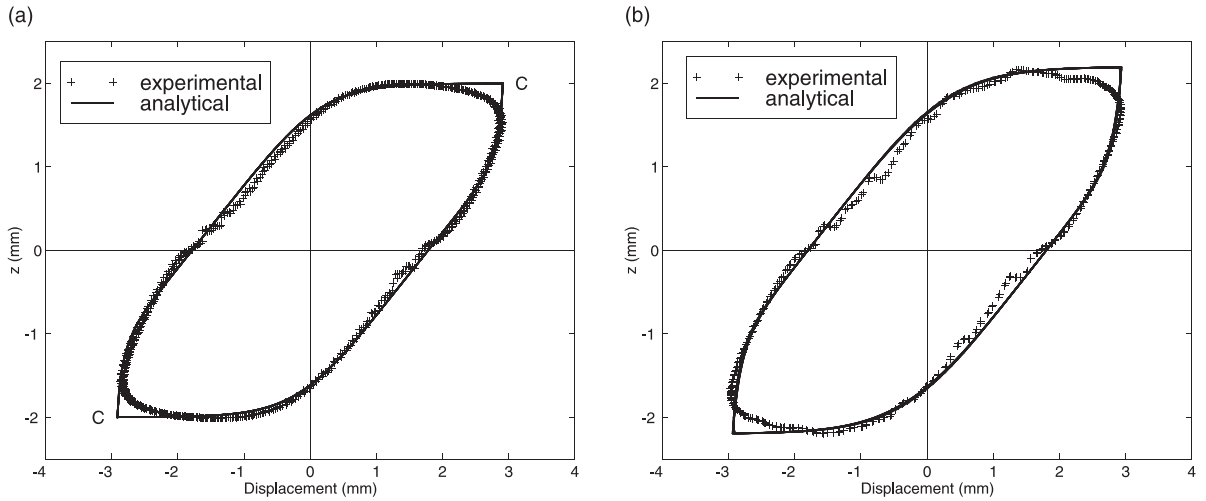

Fig. 10. The results by the Bouc–Wen model: (a) for 3 Hz excitation, and (b) for 7 Hz excitation.

Table 5
Estimated parameters for the present model by Eq. (6a)–(6c) (experimental data are used)

	Excitation frequency (Hz)	c	m	α	β	γ	n
Present model	3	0.0240	0.7973	0.8300	0.1265	−0.0352	5.1540
	5	0.0117	0.8973	0.7994	0.0992	−0.0201	4.8739
	7	0.0083	0.9165	0.7907	0.1166	−0.0265	4.5509

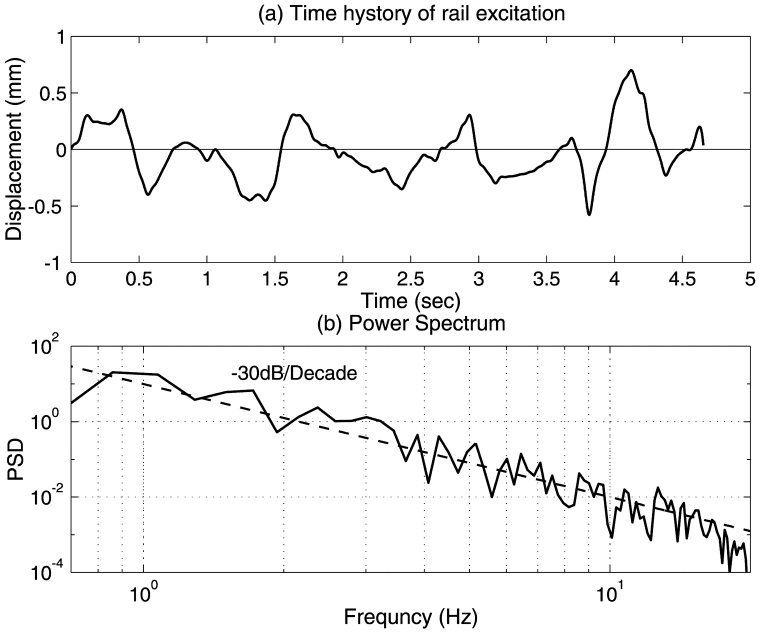

Fig. 11. Typical displacement input.

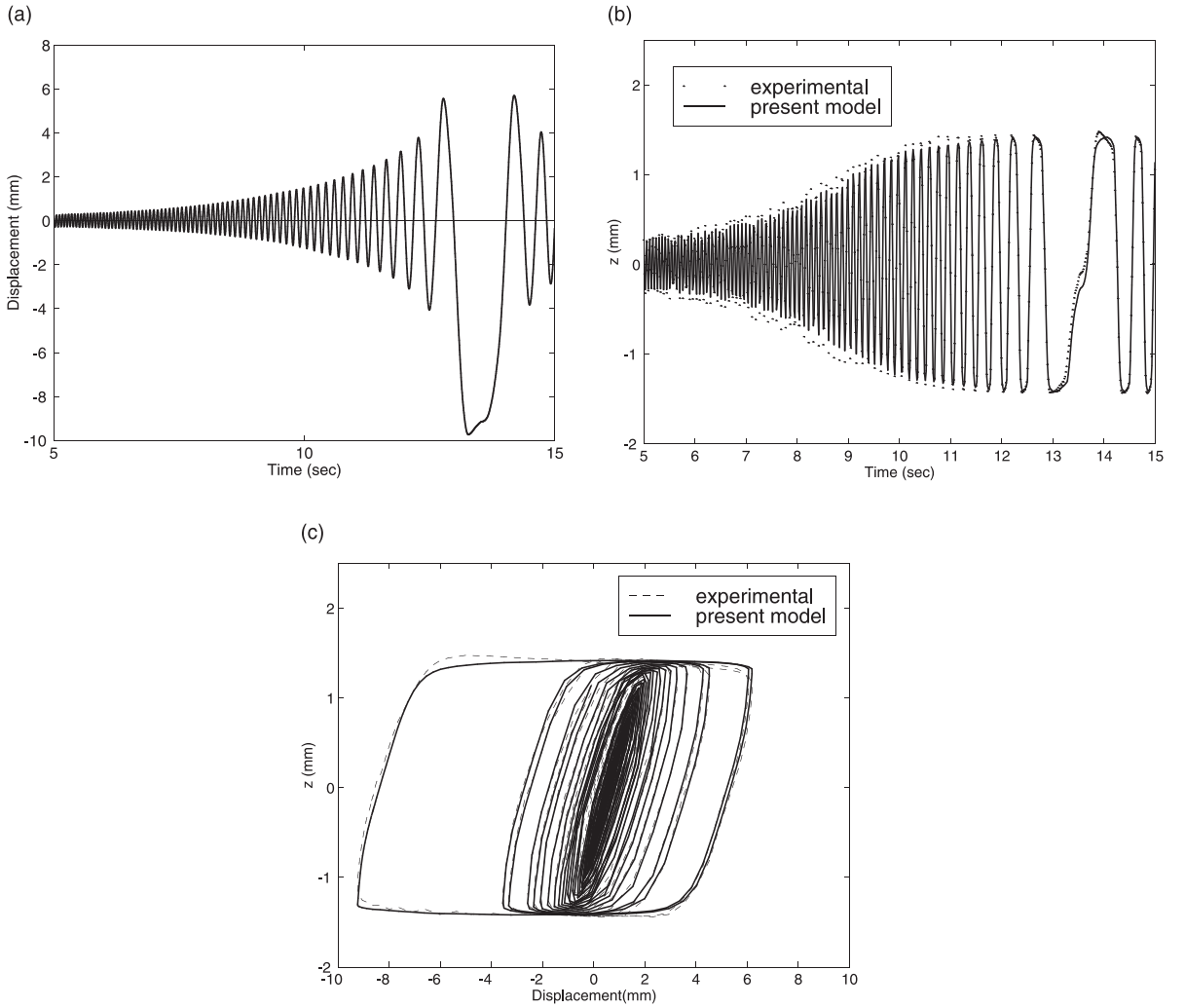

Fig. 12. Results from the multi-frequency parameter estimation: (a) time history of the swept-sinusoidal displacement input to the system, (b) time history of the experimentally measured restoring force and (c) the hysteresis loop predicted by the present nonlinear model is compared with the experimentally determined loop.

Table 6
Estimated parameters from multi-frequency excitation data shown in Fig. 12

c	m	α	β	γ	n
0.0055	0.7700	0.9614	1.1226	−0.6724	2.8639

5. Conclusions

The experimental evidence confirming nonlinear rate-dependent stick-slip phenomena in a certain rubber-to-metal interface is presented. The present generalization of the Bouc–Wen model, incorporating

a rate-dependent damping model, is shown appropriately to model the complicated nonlinear phenomena. A two-stage estimation technique is proposed for the estimation of the present nonlinear model and an effective experimental technique useful for actual multi-frequency displacement excitations is also suggested. The present nonlinear model is shown to outperform the existing Bouc–Wen model in characterizing complicated rate-dependent stick-slip phenomena.

Appendix A

The elements of the Jacobian matrix $\partial R_k/\partial\theta_i$ are as follows:

If Eq. (5) is used:

$$\frac{\partial R_k}{\partial c} = \ddot{x}_k[m|\dot{x}_k|^{m-1}\operatorname{sgn}^2(\dot{x}_k) + |\dot{x}_k|^m\delta(\dot{x}_k)],$$

$$\frac{\partial R_k}{\partial m} = c\ddot{x}_k[|\dot{x}_k|^{m-1}\operatorname{sgn}^2(\dot{x}_k) + m|\dot{x}_k|^{m-1}\ln|\dot{x}_k|\operatorname{sgn}^2(\dot{x}_k) + |\dot{x}_k|\ln|\dot{x}_k|\delta(\dot{x}_k)],$$

$$\frac{\partial R_k}{\partial \alpha} = \dot{x}_k,$$

$$\frac{\partial R_k}{\partial \beta} = -|\dot{x}_k||z_k|^{n-1}z_k,$$

$$\frac{\partial R_k}{\partial \gamma} = -\dot{x}_k|z_k|^n,$$

$$\frac{\partial R_k}{\partial n} = -[\beta|\dot{x}_k||z_k|^{n-1}z_k + \gamma\dot{x}_k|z_k|^n]\ln|z_k|.$$

If Eq. (6a)–(6c) is used:

$$\frac{\partial R_k}{\partial c} = \ddot{x}_k[m|\dot{x}_k|^{m-1}\operatorname{sgn}^2(\dot{x}_k) + |\dot{x}_k|^m\delta(\dot{x}_k)] + n|z_{\mathrm{BW},k}|^{n-1}|\dot{x}_k|^m\operatorname{sgn}(\dot{x}_k)[\beta|\dot{x}_k| + \gamma\dot{x}_k\operatorname{sgn}(\dot{x}_k)]$$

$$\frac{\partial R_k}{\partial m} = c\ddot{x}_k[|\dot{x}_k|^{m-1}\operatorname{sgn}^2(\dot{x}_k) + m|\dot{x}_k|^{m-1}\ln|\dot{x}_k|\operatorname{sgn}^2(\dot{x}_k) + |\dot{x}_k|\ln|\dot{x}_k|\delta(\dot{x}_k)] + nc|z_{\mathrm{BW},k}|^{n-1}|\dot{x}_k|^m\operatorname{sgn}(\dot{x}_k)\ln|\dot{x}_k|[\beta|\dot{x}_k| + \gamma\dot{x}_k\operatorname{sgn}(\dot{x}_k)\operatorname{sgn}(\dot{x}_k)],$$

$$\frac{\partial R_k}{\partial \alpha} = \dot{x}_k,$$

$$\frac{\partial R_k}{\partial \beta} = -|\dot{x}_k||z_{\mathrm{BW},k}|^{n-1}z_{\mathrm{BW},k},$$

$$\frac{\partial R_k}{\partial \gamma} = -\dot{x}_k|z_{\mathrm{BW},k}|^n,$$

$$\frac{\partial R_k}{\partial n} = -[\beta|\dot{x}_k||z_{\mathrm{BW},k}|^{n-1}z_{\mathrm{BW},k} + \gamma\dot{x}_k|z_{\mathrm{BW},k}|^n]\ln|z_{\mathrm{BW},k}|.$$

References

Baber, T.T., Wen, Y.K., 1981. Random vibration of hysteretic degrading systems. ASCE Journal of the Engineering Mechanics Division 107, 1069–1089.

Bouc, R., 1967. Forced vibration of mechanical system with hysteresis. In: Proceedings of the Fourth Conference on Nonlinear Oscillations. Prague, p. 315.

Chassiakos, A.G., Masri, S.F., Smyth, A.W., Caughey, T.K., 1998. On-line identification of hysteretic systems. ASME Journal of Applied Mechanics 65, 194–203.

Draper, N.R., Smith, H., 1981. Applied Regression Analysis. Wiley, New York.

Fertis, D.G., Lee, C.T., 1992. Inelastic response of variable stiffness members under cyclic loading. ASCE Journal of Engineering Mechanics 118, 1406–1440.

Fletcher, R., 1980. Practical Methods of Optimization, vol. 1. Wiley, New York.

ISO 1978. Guide for evaluation of human exposure to whole body vibration.

Kim, Y.Y., Jung, H.I., 1996. Optimization of Dynamic Characteristics of a Roller Guide system for Lateral Vibration Reduction, Technical Report. Institute of Advanced Machinery Design, Seoul National University.

Loh, C.H., Chung, S.T., 1993. A three-stage identification approach for hysteretic systems. Earthquake Engineering and Structural Dynamics 22, 129–150.

Michalakis, C.C., Tadibakhsh, I.G., 1985. Hysteretic dampers in base isolation: random approach. Journal of Structural Engineering 111, 705–721.

Miwa, T., 1967. Evaluation methods for vibration effect. In: Industrial Health, vol. 5. pp. 183–205.

Mottershead, J.E., Stanway, R., 1986. Identification of *N*th power velocity damping. Journal of Sound and Vibration 105, 309–315.

Ni, Y.Q., Ko, J.M., Wong, C.W., 1998. Identification of non-linear hysteretic isolators from periodic vibration tests. Journal of Sound and Vibration 217, 737–756.

Sissala, M., Heimola, T., Otala, M., 1985. Optimization of lift car vibrational behaviour by modal analysis. Elevator World, June 1985, pp. 27–31.

Sues, R.H., Mau, S.T., Wen, Y.K., 1988. System identification of degrading hysteretic restoring forces. ASCE Journal of Engineering Mechanics 114, 833–846.

Tinker, M.L., Cutchins, M.A., 1992. Damping phenomena in a wire rope isolation system. Journal of Sound and Vibration 157, 7–18.

Tinker, M.L., Cutchins, M.A., 1994. Instabilities in a non-linear model of a passive damper. Journal of Sound and Vibration 176, 415–428.

Vinogradov, O., Pivovarov, I., 1986. Vibration of a system with a non-linear hysteresis. Journal of Sound and Vibration 111, 145–152.

Wen, Y.K., 1976. Method of random vibration of hysteretic systems. ASCE Journal of the Engineering Mechanics Division 102, 249–263.

Wong, C.W., Ni, Y.Q., Lau, S.L., 1994a. Steady-state oscillation of hysteretic differential model. I. Response analysis. ASCE Journal of Engineering Mechanics 120, 2271–2298.

Wong, C.W., Ni, Y.Q., Ko, J.M., 1994b. Steady-state oscillation of hysteretic differential model. II. Performance analysis. ASCE Journal of Engineering Mechanics 120, 2299–2325.

Yar, M., Hammond, J.K., 1987. Parameter estimation for hysteretic systems. Journal of Sound and Vibration 117, 161–172.